ELECTRON FLUIDS

Imaging the breaking of electrostatic dams in graphene for ballistic and viscous fluids

Zachary J. Krebs[1]†, Wyatt A. Behn[1]†, Songci Li[1], Keenan J. Smith[1], Kenji Watanabe[2], Takashi Taniguchi[3], Alex Levchenko[1], Victor W. Brar[1]*

The charge carriers in a material can, under special circumstances, behave as a viscous fluid. In this work, we investigated such behavior by using scanning tunneling potentiometry to probe the nanometer-scale flow of electron fluids in graphene as they pass through channels defined by smooth and tunable in-plane p-n junction barriers. We observed that as the sample temperature and channel widths are increased, the electron fluid flow undergoes a Knudsen-to-Gurzhi transition from the ballistic to the viscous regime characterized by a channel conductance that exceeds the ballistic limit, as well as suppressed charge accumulation against the barriers. Our results are well modeled by finite element simulations of two-dimensional viscous current flow, and they illustrate how Fermi liquid flow evolves with carrier density, channel width, and temperature.

The interactions between particles that make up a fluid play a critical role in how the fluid flows. At low densities, where the particles are free to move ballistically, such as in gases, the conductance of a constriction is dependent on only the channel width and particle scattering from the walls, which leads to momentum loss. At higher densities, interactions between particles—which preserve momentum—become more frequent and can lead to collective flows that enhance conductance through the constriction beyond the ballistic limit (*1*, *2*). This phenomenon, which is exhibited by viscous fluids with laminar flow, was predicted by Gurzhi to also occur in electronic systems when the electron-electron (e-e) scattering length l_{ee} becomes shorter than the momentum-relaxing scattering length l_{mr} stemming from electron-impurity and electron-phonon scattering (*3*, *4*). Initially, signatures of this effect were observed in high-mobility gallium arsenide quantum wells and wires, manifested by a decrease of resistance with an increase of temperature (*5*–*7*) as well as other electron fluid–like behaviors (*8*–*11*).

The focus of recent attention on hydrodynamic phenomena largely concerns graphene, other two-dimensional (2D) van der Waals materials, and topological semimetals, where short e-e mean free paths and low Umklapp scattering rates allow the quasiparticles to form strongly correlated viscous Fermi or Dirac fluids (*12*–*31*). The range of hydrodynamic behaviors that are predicted to occur in these viscous fluid states include current vortex formation (*15*, *16*), higher-than-ballistic conduction (*17*, *18*), strong nonlocality (*22*–*24*), and anomalous thermoelectric responses (*25*–*28*). To observe these effects, several experimental methods have been implemented. Transport measurements through a series of lithographed constrictions and strategically contacted samples have recently observed signatures of superballistic conductance as well as negative nonlocal resistance (*32*–*34*). In a parallel vein, a departure from the Mott relations, a giant violation of the Wiedemann-Franz law, and breakdown of Matthiessen's rule were observed in the hydrodynamic regime in graphene (*35*, *36*). Meanwhile, scanned single electron transistor and nitrogen vacancy measurements of etched, encapsulated graphene devices have imaged Poiseuille current density profiles—a hallmark of viscous flow—in Hall bar and Corbino geometries (*37*–*41*). And, very recently, a scanned SQUID (superconducting quantum interference device) imaging technique has enabled visualization of current whirlpools in tungsten ditelluride (*42*). Lastly, Kelvin probe force microscopy has been used to image, with 60-nm resolution, regions

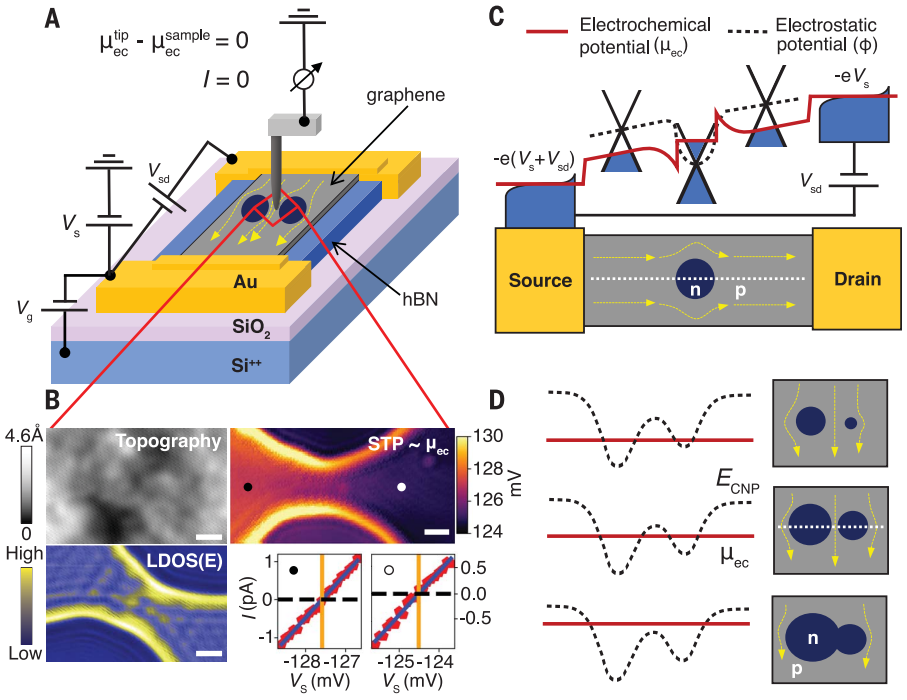

Fig. 1. Experimental method for imaging charge flow through variable-width channels. (**A**) Schematic of the STP experimental setup. V_{sd} drives current through the sample, and V_s (I = 0) determines the difference between the sample and tip electrochemical potentials. The carrier density (and E_F) is globally modified with an electrostatic gate electrode V_g. (**B**) Simultaneously acquired topography (top left) and electronic local density of states (LDOS) (bottom left) (V_s = −10 mV, V_g = −2 V) of the electrostatic dam. (Top right) Example STP map (V_g = −2 V) of the same area acquired under transport. All scale bars are 100 nm. (Bottom right) Example tunneling I-V curves recorded at two points shown on the STP map. I = 0 (black dashed line) determines the local electrochemical potential $\mu_{ec} = -V_s$ (orange vertical line) of the sample; by fitting many such curves (blue solid line), μ_{ec} is mapped spatially. (**C**) An energy diagram depicting how the electrostatic and electrochemical potentials vary along the flow direction across a potential well (white dashed line). The variations in μ_{ec} near the scatterer are exaggerated for clarity. (**D**) Schematic of an electrostatic dam at several gating conditions. The size of two p-n junction barriers increases from high to low hole doping (top to bottom), closing off the channel between them and blocking the flow of current. The leftmost panels show the local charge neutrality point (E_{CNP}) and μ_{ec} along the white dashed line. E_{CNP} follows the in-plane electrostatic potential defining the dam.

[1]Department of Physics, University of Wisconsin–Madison, Madison, WI 53706, USA. [2]Research Center for Functional Materials, National Institute for Materials Science, Tsukuba 305-0044, Japan. [3]International Center for Materials Nanoarchitectonics, National Institute for Materials Science, Tsukuba 305-0044, Japan.
*Corresponding author. Email: vbrar@wisc.edu
†These authors contributed equally to this work.

of negative local resistance in chemical vapor–deposited graphene on silicon dioxide that were attributed to viscous flow behavior around intrinsic defects (*43*).

In this work, we used scanning tunneling potentiometry (STP) to image, with nanometer-scale spatial resolution, the electrochemical potential profile associated with quasiparticle flow in graphene around electrostatic barriers that are "drawn" using voltage pulses from the tip of a scanning tunneling microscope (STM) (*44*). This methodology allows for the creation of smooth barriers defined by in-plane p-n junctions, which confine the particle flow without introducing diffusive scattering or other momentum-relaxing processes that occur at the edges of lithographed samples (*45*, *46*). Moreover, we were able to vary the width of the conduction channels from micrometer scale to pinch-off (where the barriers form "electrostatic dams" that suppress flow) by tuning the carrier density. Another distinguishing feature of our experiment is that the graphene/hexagonal boron nitride (hBN) samples that we probed were nonencapsulated, which serves to reduce dielectric screening and therefore enhance e-e interactions, allowing viscous flow to be observed at shorter length scales.

Imaging and quantifying charge flow using STP

A schematic of our STP measurement geometry is shown in Fig. 1A. In STP, a source-drain bias (V_{sd}) is used to drive current through a thin sample, and the subsequent spatially varying electrochemical potential (μ_{ec}) is measured locally using an STM tip (*47*–*51*). To measure μ_{ec}, the feedback of the STM tip is turned off, and the tip bias needed to zero the tunneling current (I) is determined by performing a linear fit of the tunneling current-voltage (I-V) curve (Fig. 1B). This allows μ_{ec} to be determined to within ~10 μV and at the angstrom-scale spatial resolution of standard STM. Figure 1C illustrates how μ_{ec} varies across the sample under transport conditions and in the presence of a p-n junction, which scatters incident carriers. When $V_{sd} = 0$, all local accumulations of charge that affect the chemical potential, or Fermi level (E_F), are offset by changes in electrostatic potential ϕ, such that $\mu_{ec} = \phi + E_F$ is constant across the surface. For $V_{sd} \neq 0$, however, μ_{ec} will change continuously across the sample, with a spatially varying slope that depends on the local conductivity; meanwhile, any changes in local charge accumulation that are caused by active carrier scattering or ballistic transport will also affect μ_{ec} and be detectable with STP (*51*–*54*).

Previous STP measurements of graphene devices on silicon carbide (SiC) substrates have revealed sharp drops in potential associated with monolayer-bilayer boundaries, as well as subsurface crystal steps. In some cases, Landauer residual resistivity dipoles (LRRDs) were observed near defect features, which could be used to model the electron-barrier scattering mechanisms (*55*–*61*). STP measurements have also been performed on graphene nanoribbons on SiC in the ballistic transport regime (*62*). The use of SiC as a substrate, with its large dielectric constant, strongly screens e-e interactions and therefore suppresses hydrodynamic effects. Those measurements also used topographic features to act as scattering barriers, which are known to introduce artifacts into STP measurements owing to tip convolution (*63*).

In this work, we probed monolayer graphene/hBN samples with electrostatic barriers that were introduced by "drawing" them with the STM tip using a previously developed methodology (*44*, *64*, *65*). Each barrier was created by introducing subsurface charges in the underlying hBN by applying a 1- to 2-min, 5-V pulse with the STM tip. This technique creates an electrostatic potential well in the plane of the graphene sheet that scatters incident holes and electrons. Within a suitable range of negative gate voltages, a circular p-n (outside-inside) junction forms on the periphery of the potential well, which acts as a reflective boundary for graphene quasiparticles (*66*). By placing two of these p-n junctions in proximity, we built a small channel that current can flow through when a source-drain bias is applied. Moreover, as shown in Fig. 1D, the width of this current-carrying channel can be tuned by using an electrostatic back gate to adjust E_F, which alters the radii of the p-n junction barriers; the p-n junctions considered here decrease in radius with higher hole concentrations, which leads to an increased channel width. Prior to introducing the barriers, STP measurements of transport

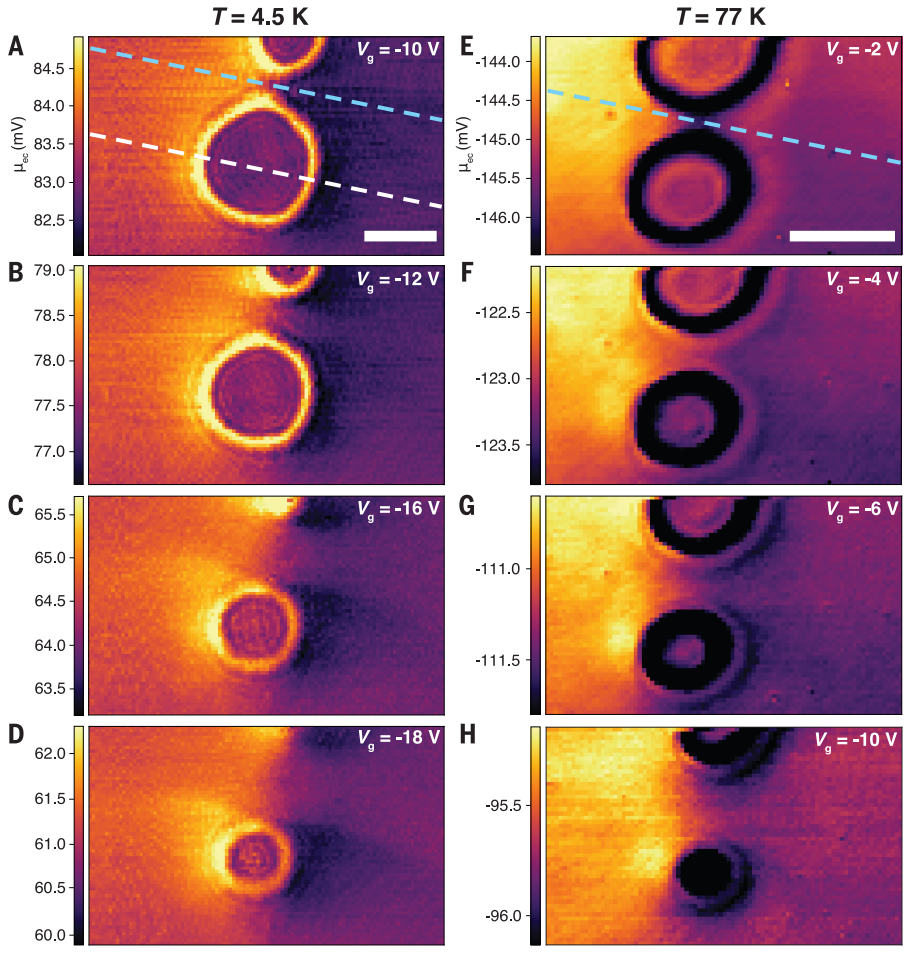

Fig. 2. Mapping the electrochemical potential near electrostatic dams at low and high temperature. (**A** to **D**) STP maps of an electrostatic dam at T = 4.5 K, V_{sd} = 0.4 V, and four selected gate voltages: −10, −12, −16, and −18 V, in order of increasing channel width. (**E** to **H**) STP maps of a second electrostatic dam at T = 77 K, V_{sd} = −0.4 V, and four gate voltages: −2, −4, −6, and −10 V, in order of increasing channel width. The scale bars are 250 nm. The direction of incident current flow for all images is from left to right along the dashed lines in (A) and (E), which are used later to plot linecuts of μ_{ec} in Fig. 3.

across the bare surface were performed to obtain the potential drop caused solely by momentum-relaxing scattering sources, which was then used to calculate l_{mr} = 5 μm at 4.5 K (*67*).

Mapping the electrochemical potential drop near barriers

STP images acquired after the formation of the potential wells at 4.5 and 77 K are shown in Fig. 2. At both 4.5 and 77 K, μ_{ec} is observed to increase (decrease) on the upstream (downstream) side of the potential wells, creating in-plane dipoles. We identify these features as LRRDs, which are known to occur in ballistic or near-ballistic transport conditions when scattered charge carriers accumulate (deplete) on the upstream (downstream) side of a barrier (*47*). To better visualize this behavior, cross-sectional cuts across the barriers are shown in Fig. 3, A and B, which capture the effect of the charge accumulation on μ_{ec}. At 4.5 K, we find that the changes in μ_{ec} in both the accumulation and depletion zones can be fit well with a R^{-1} dependence, where R is the distance from the center of the barrier, in good agreement with LRRD theory for ballistic transport (*68*, *69*). A more detailed, full image of the theoretical LRRD for ballistic transport in a 2D system is shown in Fig. 3C, which was calculated using a framework introduced in (*70*) and described in (*67*). The dipole profile at 77 K shows a notable difference (Fig. 3B): The accumulation and depletion profiles are decreased in magnitude by a factor of ~2.5 from those at 4.5 K. The decreased dipole strength at high temperatures can be explained in terms of viscous corrections to the electronic flow. Guo *et al.* showed that frequent e-e interactions reduce the effective scattering strength of obstacles seen by incident charge carriers (*70*). This is because electrons reflected by an obstacle can receive momentum from incoming electrons back in the direction of current flow, keeping them from fully backscattering. The magnitude of this dipole reduction can be modeled as a function of the quantity r/l_{ee}, where r is the scattering length of a barrier and is approximately equal to the barrier radius. Figure 3D shows the predicted dipole potential profile on one side of the barrier as a function of l_{ee}, plotted alongside the experimental data. The observed reduction in dipole strength at 77 K is consistent with $r/l_{ee} \sim 1$, which corresponds to $\tilde{l}_{ee}$ = 150 nm. We denote this experimentally derived value of l_{ee} with a tilde because this value is only accurate up to a multiplicative factor of order one owing to uncertainty in the scattering length r.

Within the quantum wells, meanwhile, the STP images reveal standing waves associated with circular quasibound states trapped in the well. These states are excited by the incident current-carrying carriers, creating changes to the local charge density that are visible in STP (*53*). The p-n barrier can be observed as the bright (dark) ring in the 4.5 K (77 K) measurements. The same ring feature has been determined in previous scanning tunneling spectroscopy and Kelvin probe force microscopy measurements to indicate the position of the classical turning point of the quasi-bound states, where there is an accumulation

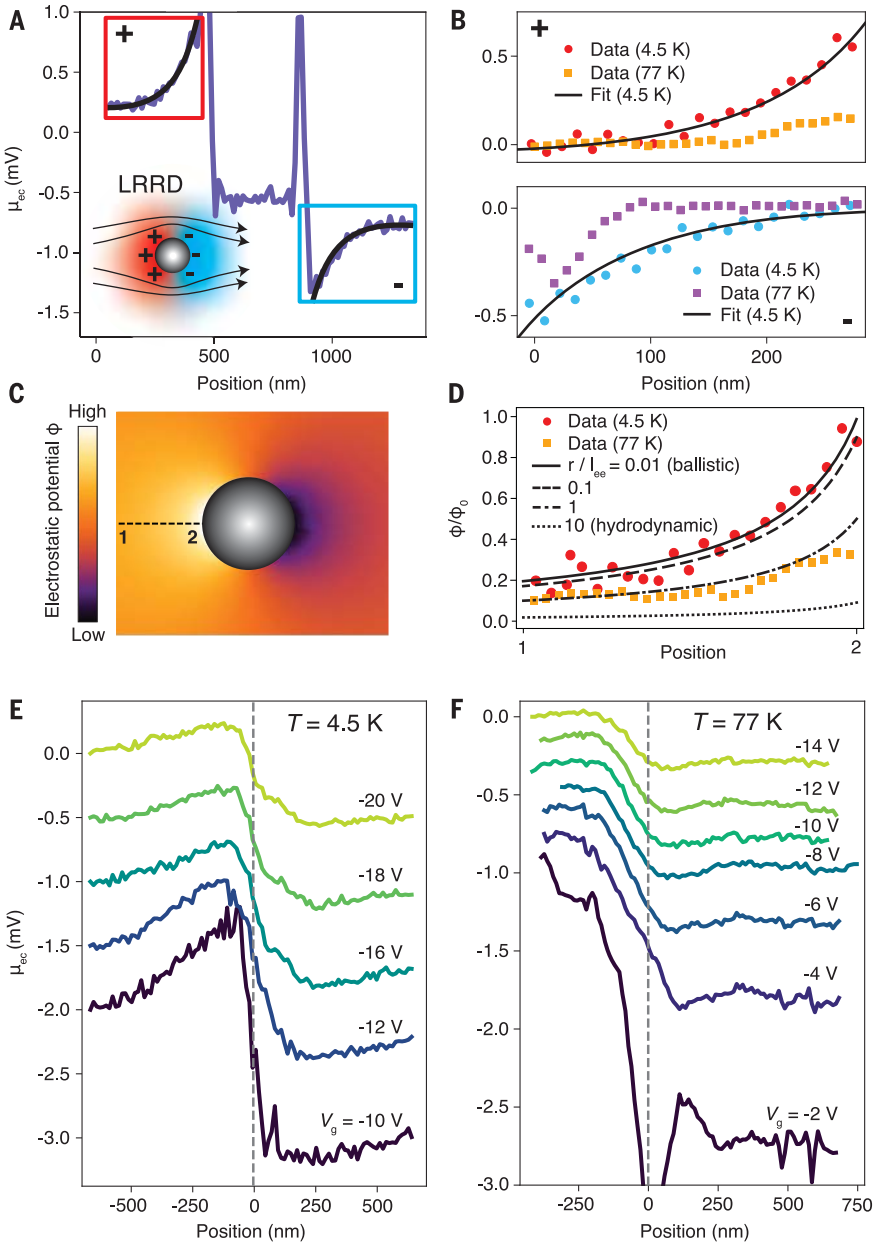

Fig. 3. Tracking the gate-dependent voltage drop through the channels and formation of LRRDs across the electrostatic barriers. (**A**) Linecut along the white dashed line in Fig. 2A revealing the LRRD structure at T = 4.5 K. Data within the red (blue) box corresponds to an accumulation (depletion) of holes. (**B**) (Top) Zoom-in of the accumulation zone in (A). (Bottom) Zoom-in of the depletion zone in (A). Both are plotted alongside the equivalent linecuts at 77 K. Solid lines show R^{-1} fits to the 4.5 K data. (**C**) Predicted electrostatic potential of an LRRD around a circular obstacle when current is flowing from left to right (*67*). (**D**) Normalized linecuts of the electrostatic potential in (C) for varying e-e scattering lengths, parameterized by r/l_{ee} and compared with the data from (B). (**E**) Linecuts along the blue dashed line in Fig. 2A at T = 4.5 K. (**F**) Linecuts through the blue dashed line in Fig. 2E at T = 77 K.

of quasiparticle density (*44*, *71*–*73*). It is not fully understood why the p-n boundary appears bright for measurements at 4.5 K but dark at 77 K. This effect was observed in multiple separate measurements, and we speculate that STP is sensitive to thermovoltages generated on the p-n boundary because of strong tip-induced resonances in the local density of states (*72*, *74*, *75*). Figure S3 shows how the p-n junctions change appearance in response to heating.

In addition to the features described above, we also observe a drop in μ_{ec} along a path through the channel between the wells in the direction of current flow, which represents a central focus of this work. This change in μ_{ec} is associated with current that flows through the channel, the width of which can be tuned via electrostatic gating (as illustrated in Fig. 1D). Figure 2 shows how μ_{ec} evolves in the vicinity of the channels as their width is varied from as wide as 400 nm to pinch-off, where it forms an electrostatic dam that blocks the incident current. At 4.5 K, raylike "streams" of current are visible emerging from the downstream side of the channel, a property that is consistent with ballistic carriers passing through the gap and locally increasing μ_{ec} (*54*, *76*). Such qualitative streams are not as apparent for data obtained at 77 K. To quantify the potential drop induced by the channels, we recorded μ_{ec} along linecuts through the channels along the direction of current flow (Fig. 3, E and F). At both low and high measurement temperatures, an increase in hole carrier density at lower gate voltages is associated with a smaller potential drop through the channels. This trend is expected, because a larger carrier density both widens the channel and increases the conductivity of graphene, creating a more conductive channel overall. We also note that the potential drop in the 4.5 K data is highly symmetric about the channel midpoint, whereas in the 77 K data, the potential drop seems to occur mostly on one side (to the left of the vertical dashed line in Fig. 3F). We attribute this to a slight misalignment of the incident current direction with the channel axis.

Channel conductances

To quantitatively characterize the carrier flow, we used the measured electrochemical drop ($\Delta\mu_{ec}$) through the channels (Fig. 3, E and F) to calculate the conductance of each channel, $G_{data} = I_{channel}/\Delta\mu_{ec}$. The current flowing through each channel ($I_{channel}$) is first estimated using the assumption that the ratio between the channel width (w) and the width of the graphene flake (W = 15 μm) is proportional to the ratio between $I_{channel}$ and the current passing through the whole flake (J), measured using an ammeter—that is, $w/W = \alpha I_{channel}/J$. The proportionality constant α depends on the precise boundary conditions and geometry of our sample, as well as on any deflection of current caused by the perturbing potential of the STM tip (*66*). Although α cannot be calculated a priori, it can be estimated by comparing our data at 4.5 K to the Sharvin formula for ballistic transmission through a channel

$$G_{Sh} = G_Q \frac{\overline{E_F}}{\pi\hbar v_F} w \qquad (1)$$

where $\hbar$ is Planck's constant (h) divided by 2π, $G_Q = 4e^2/h$ is the conductance quantum, w is the minimum width inside the channel, v_F is the Fermi velocity, and $\overline{E_F}$ is the Fermi level (chemical potential) averaged over the narrowest cross section of the channel. In repeated measurements at 4.5 K using a new electrostatic dam each time, we find excellent agreement between G_{Sh} and G_{data} for channel widths up to 400 nm when α = 2.8, as shown in Fig. 4A. This agreement is expected, given that the only changes between subsequent measurements are slight variations in the tip potential near its apex and the positioning of our electrostatic dams within the center of the graphene flake. For w > 400 nm, the Sharvin prediction is consistently less than the measured conductance, because the geometry starts to resemble two separate barriers instead of a well-defined channel (*67*). In contrast to measurements at 4.5 K, data taken at 77 K demonstrate a channel conductance that is larger than the ballistic Sharvin prediction with α = 2.8, and this deviation increases as the channel is widened. Simply adjusting α as a fitting parameter does not produce good agreement between the data at 77 K and the ballistic theory across all channel widths (*67*). This suggests that a viscous Gurzhi contribution (G_G)—which is known to depend quadratically on channel width (*17*)—should be added to the channel conductance at elevated temperatures. Notably, modeling the viscous corrections to the channel conductance only requires the addition of a single term to the Sharvin formula. This additive correction can be qualitatively understood in the following way: When e-e interactions are prevalent, charge carriers that are backscattered by the channel edges now experience forward scattering processes that push them back through the channel, which in effect increases the number of conduction channels beyond the Sharvin limit (*18*). To account for this viscous contribution and provide another experimental estimate of the e-e scattering length l_{ee}, we turn to (*17*, *32*)

$$G = G_{Sh} + G_G, G_G = c_G G_Q \frac{\overline{E_F}}{\pi\hbar v_F} \frac{w^2}{l_{ee}} \qquad (2)$$

which holds in the absence of significant momentum-relaxing scattering processes (*76*). From Eq. 2, we can write

$$l_{ee} = c_G w \left(\frac{G_{data}}{G_{Sh}} - 1 \right)^{-1} \qquad (3)$$

where c_G is a nonuniversal numerical factor that is specific to viscous flow around our electrostatic dams. For example, $c_G = \pi^2/16 = 0.62$ for a perfect slit geometry (*17*); however, the value of c_G also depends on the boundary conditions and differs for flows with no-slip and no-stress conditions (*45*, *46*, *77*, *78*). For our geometry, we expect c_G = 0.75 on the basis of viscous fluid simulations described below [also, see (*67*)]. The resulting theoretical channel conductance is plotted in Fig. 4A, showing good agreement with 77 K measurements and providing strong evidence of viscous effects in the electron fluid increasing the channel conductance. Corresponding estimates of l_{ee} using Eq. 3 are shown in Fig. 4B, giving values that are

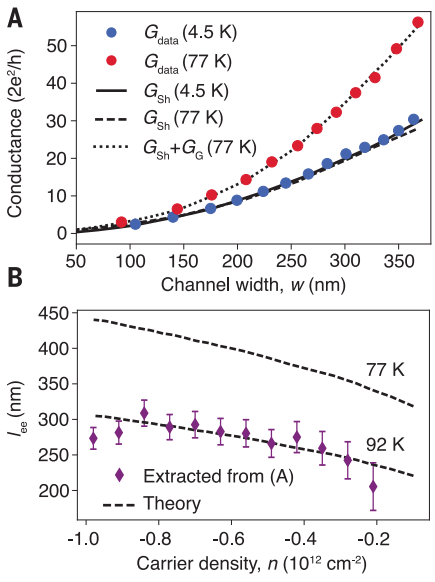

Fig. 4. Channel conductances and extracted electron-electron scattering lengths. (**A**) Channel conductance $G_{data} = I_{channel}/\Delta\mu_{ec}$ obtained from the STP data at both low (blue, 4.5 K) and high (red, 77 K) temperature. Theoretical curves (solid and dashed lines) are calculated using the Sharvin formula (Eq. 1). A viscous contribution G_G is included in the dotted line. (**B**) e-e scattering lengths extracted from the red (77 K) data points and the dotted fit in (A) using Eq. 3. Values for the dashed theory curves were taken from the microscopic calculations in (*14*). Error bars on the data points come from a 14-nm uncertainty in the channel widths, w. All data points presented in this figure were obtained from a repeated set of STP measurements distinct from those in Fig. 2. The results from a similar analysis of Fig. 2 are found in (*67*) and closely replicate the above results.

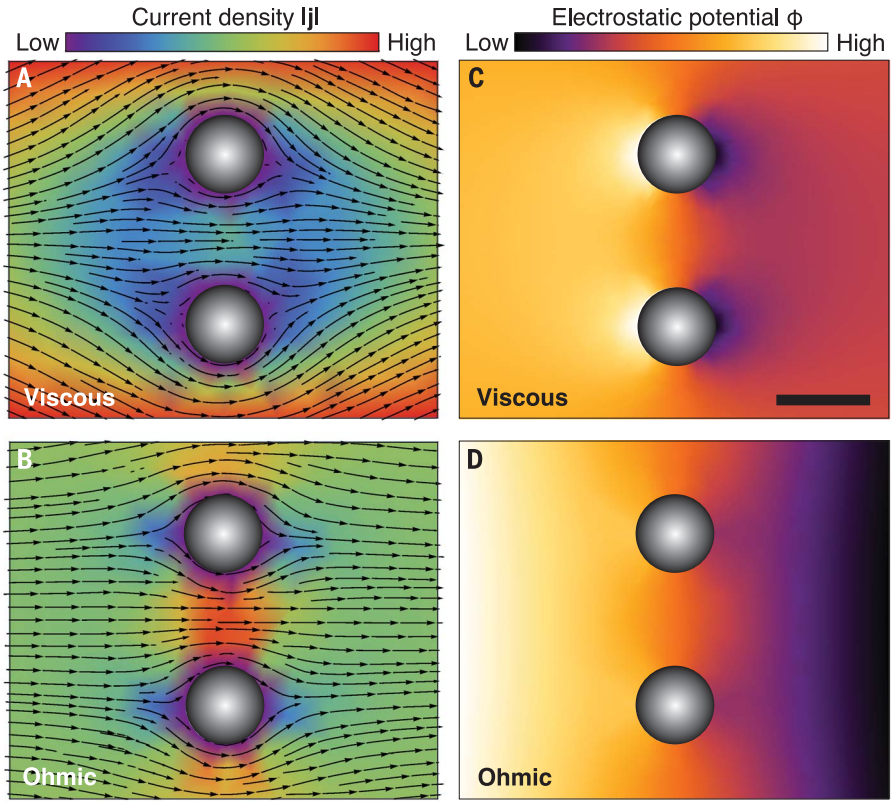

Fig. 5. Finite element models of carrier flow in the ohmic and viscous regimes. Numerical solutions for the current density and electric potential describing hydrodynamic flow through two circular barriers in the viscous regime (top panels) and ohmic regime (bottom panels). (**A** and **B**) The arrow plots show the streamline of the current density, and the color plots show the magnitude of the current density. (**C** and **D**) Electrostatic potential induced by current flow corresponding to the viscous and ohmic cases in (A) and (B), respectively. The scale bar is 250 nm.

shorter than previous measurements of hBN-encapsulated graphene largely because of the weaker dielectric environment ε of our samples (*32*). In Fig. 4B, we also plot theoretically predicted values of l_{ee} taken from (*14*) after multiplying by the factor $(\varepsilon/\varepsilon_{enc})^2 = (2.5/4)^2 = 0.39$ to account for the reduced dielectric screening of e-e interactions, where $\varepsilon_{enc} = 4$ is the dielectric constant for encapsulated samples (*14*). We note that for a temperature of $T = 77$ K, the measured scattering lengths l_{ee} are still less than the predicted value by ~30%, and we obtain a good fit using a temperature of 92 K (assuming $l_{ee} \sim T^{-2}$). This difference could be a result of multiple effects, such as Joule heating or a nonequilibrium energy distribution of electrons. Other factors include STM tip–induced gating effects and uncertainty in our estimate of c_G, which is known to depend sensitively on the channel boundary conditions.

Simulating carrier flow

These findings indicate that as the temperature of the graphene is increased from 4.5 K to 77 K, l_{ee} decreases until it is comparable to the width of the channel. Under these conditions, the carrier flow transitions from the Knudsen to the Gurzhi regime, where it behaves as a viscous Fermi liquid and exhibits superballistic conductance through a channel. To better understand the potential profiles measured using STP and how they relate to viscous flow, we compared our measurements with the following theoretical model. The motion of hydrodynamic electron flow under moderate external drive can be described by the linear Navier-Stokes equation in the following form

$$\nu\nabla^2\mathbf{u} - \frac{\mathbf{u}}{\tau_{mr}} = \frac{e}{m}\nabla\phi \qquad (4)$$

where $\mathbf{u}$ is the macroscopic flow velocity, τ_{mr} is the momentum relaxation time, ν is the kinematic viscosity of the electron fluid, e is the carrier charge, m is the carrier mass, and ϕ is the electric potential. The first term on the left-hand side of Eq. 4 describes viscous stress, while the second term accounts for ohmic loss. In addition, the continuity equation for current conservation is written as

$$\nabla\cdot\mathbf{j} = 0 \qquad (5)$$

Considering that $\mathbf{j} = ne\mathbf{u}$ and assuming constant electron density n, the linear Navier-Stokes Eq. 4 is recast in the form

$$l_G^2\nabla^2\mathbf{j} - \mathbf{j} = \sigma\nabla\phi \qquad (6)$$

where σ is the Drude conductivity (*67*). The interplay of viscous and momentum-relaxing terms introduces a natural length scale in the problem, namely the Gurzhi length, $l_G \equiv \sqrt{\nu\tau_{mr}} = \sqrt{l_{ee}l_{mr}}/2$. If $l_G \ll w$, where w is the typical size of the system, such as the width of the channel, the viscous stress in Eq. 6 can be neglected and the fluid enters the ohmic regime. In contrast, if $l_G \gg w$, the ohmic dissipation in Eq. 6 is small and the system is in the viscous regime.

In this framework, Eqs. 5 and 6 allow for calculations of the current density and electric potential profiles. Whereas analytical solutions are difficult to obtain for arbitrary geometries, numerical solutions using finite element methods can be obtained for hydrodynamic flow bypassing two circular barriers. Starting from the experimentally derived scattering lengths $l_{mr} = 5$ μm and $l_{ee} = 300$ nm, we simulated a viscous fluid with Gurzhi length of order $l_G = 1$ μm > w and compared these results with current flow in the ohmic regime, $l_G = 30$ nm < w. The distribution of current density and the electric potential from these two simulations are shown in Fig. 5. In these numerical simulations, we used no-slip boundary conditions for the flow velocity $\mathbf{u}$, and the flow is driven by the bias voltage V_{sd} applied to the left side of the sample (the right side is grounded to zero).

The results shown in Fig. 5C demonstrate good qualitative agreement with the 77 K STP measurements in Fig. 2, E to G. In particular, the streams of current that are anticipated for ballistic transport are not observed in the simulated viscous flow potentials; this observation is consistent with previous simulations of Boltzmann transport theory in graphene (*76*). Moreover, our numerical simulations predict the formation of cross-barrier dipoles in the electric potential profile in the viscous regime, which are observed in the measurements. The possibility of such dipole formation near channel edges in viscous electronic fluids was previously predicted (*17*) using analytical methods; this behavior can be attributed to the fact that the electric fields near the edges point against the current flow in order to push the electron liquid away from the boundary walls. The profiles of these regions of charge accumulation

or depletion depart in magnitude from what is expected for ballistic transport. This prediction compares well with our 77 K measurements and with our analytical modeling of the dipole described in Fig. 3, where we observe and calculate reduced dipole magnitudes.

Our numerical simulations also provide simultaneous measures of the cross-channel potential drop as well as the channel current, which, combined, allow for determination of the nonuniversal viscous contribution factor, c_G, used in Eqs. 2 and 3. To obtain c_G, we performed identical numerical simulations of a narrow-slit geometry, where c_G is known analytically to be $\pi^2/16$, and compared the observed channel conductance in that simulation to the results shown in Fig. 5, A and C, yielding $c_G = 0.75$ (*67*).

Outlook

We have shown that STP can be used to visualize hydrodynamic effects in graphene through direct imaging of the local electrochemical potential while a current is passed through the graphene sheet. This methodology offers a spatial resolution superior to that of other scanned probe measurements and allows for the creation and analysis of intricate flow geometries defined by smooth barriers created by in-plane p-n junctions. In this work, we used STP to reveal superballistic conductance through narrow channels in graphene, as well as local dipoles that form in both ballistic and viscous regimes owing to local carrier accumulation. These results provide insight into the electronic transport of hydrodynamic Fermi fluids. Specifically, the reduced dipoles that we observe indicate how the overall voltage drop generated by the summation of in-plane dipoles is naturally smaller in the viscous regime than in the ballistic regime, leading to a higher overall conductance in the viscous case. These measurements also provide a framework for analyzing more-complex flow patterns that are engineered to exhibit exotic effects, such as nonreciprocal flow (*79*). Angstrom-scale images, meanwhile, could be used to visualize atomistic transport features that are predicted to occur along grain boundaries and near defects (*53*).

REFERENCES AND NOTES

1. M. Knudsen, *Ann. Phys.* **28**, 75–130 (1909).
2. Y. V. Sharvin, *Sov. Phys. JETP* **21**, 655–656 (1965).
3. R. Gurzhi, *Sov. Phys. JETP* **17**, 521–522 (1963).
4. R. Gurzhi, *Sov. Phys. Usp.* **11**, 255–270 (1968).
5. L. W. Molenkamp, M. J. M. de Jong, *Phys. Rev. B* **49**, 5038–5041 (1994).
6. M. J. M. de Jong, L. W. Molenkamp, *Phys. Rev. B* **51**, 13389–13402 (1995).
7. X. P. A. Gao *et al*., *Phys. Rev. Lett.* **94**, 086402 (2005).
8. B. A. Braem *et al*., *Phys. Rev. B* **98**, 241304 (2018).
9. A. D. Levin, G. M. Gusev, E. V. Levinson, Z. D. Kvon, A. K. Bakarov, *Phys. Rev. B* **97**, 245308 (2018).
10. G. M. Gusev, A. S. Jaroshevich, A. D. Levin, Z. D. Kvon, A. K. Bakarov, *Sci. Rep.* **10**, 7860 (2020).
11. A. Gupta *et al*., *Phys. Rev. Lett.* **126**, 076803 (2021).
12. M. Müller, J. Schmalian, L. Fritz, *Phys. Rev. Lett.* **103**, 025301 (2009).
13. I. Torre, A. Tomadin, A. K. Geim, M. Polini, *Phys. Rev. B* **92**, 165433 (2015).
14. A. Principi, G. Vignale, M. Carrega, M. Polini, *Phys. Rev. B* **93**, 125410 (2016).
15. F. M. D. Pellegrino, I. Torre, A. K. Geim, M. Polini, *Phys. Rev. B* **94**, 155414 (2016).
16. L. Levitov, G. Falkovich, *Nat. Phys.* **12**, 672–676 (2016).
17. H. Guo, E. Ilseven, G. Falkovich, L. S. Levitov, *Proc. Natl. Acad. Sci. U.S.A.* **114**, 3068–3073 (2017).
18. A. Stern *et al*., *Phys. Rev. Lett.* **129**, 157701 (2022).
19. B. N. Narozhny, I. V. Gornyi, A. D. Mirlin, J. Schmalian, *Ann. Phys.* **529**, 1700043 (2017).
20. A. Lucas, K. C. Fong, *J. Phys. Condens. Matter* **30**, 053001 (2018).
21. D. Y. H. Ho, I. Yudhistira, N. Chakraborty, S. Adam, *Phys. Rev. B* **97**, 121404 (2018).
22. G. Falkovich, L. Levitov, *Phys. Rev. Lett.* **119**, 066601 (2017).
23. A. Shytov, J. F. Kong, G. Falkovich, L. Levitov, *Phys. Rev. Lett.* **121**, 176805 (2018).
24. S. Danz, M. Titov, B. N. Narozhny, *Phys. Rev. B* **102**, 081114 (2020).
25. M. S. Foster, I. L. Aleiner, *Phys. Rev. B* **79**, 085415 (2009).
26. A. Lucas, J. Crossno, K. C. Fong, P. Kim, S. Sachdev, *Phys. Rev. B* **93**, 075426 (2016).
27. M. Zarenia, A. Principi, G. Vignale, *2D Mater.* **6**, 035024 (2019).
28. S. Li, A. Levchenko, A. V. Andreev, *Phys. Rev. B* **102**, 075305 (2020).
29. A. Levchenko, J. Schmalian, *Ann. Phys.* **419**, 168218 (2020).
30. J. Gooth *et al*., *Nat. Commun.* **9**, 4093 (2018).
31. U. Vool *et al*., *Nat. Phys.* **17**, 1216–1220 (2021).
32. R. Krishna Kumar *et al*., *Nat. Phys.* **13**, 1182–1185 (2017).
33. D. A. Bandurin *et al*., *Science* **351**, 1055–1058 (2016).
34. D. A. Bandurin *et al*., *Nat. Commun.* **9**, 4533 (2018).
35. J. Crossno *et al*., *Science* **351**, 1058–1061 (2016).
36. F. Ghahari *et al*., *Phys. Rev. Lett.* **116**, 136802 (2016).
37. J. A. Sulpizio *et al*., *Nature* **576**, 75–79 (2019).
38. L. Ella *et al*., *Nat. Nanotechnol.* **14**, 480–487 (2019).
39. A. Jenkins *et al*., *Phys. Rev. Lett.* **129**, 087701 (2022).
40. M. J. H. Ku *et al*., *Nature* **583**, 537–541 (2020).
41. C. Kumar *et al*., *Nature* **609**, 276–281 (2022).
42. A. Aharon-Steinberg *et al*., *Nature* **607**, 74–80 (2022).
43. S. Samaddar *et al*., *Nano Lett.* **21**, 9365–9373 (2021).
44. J. Velasco Jr. *et al*., *Nano Lett.* **16**, 1620–1625 (2016).
45. E. I. Kiselev, J. Schmalian, *Phys. Rev. B* **99**, 035430 (2019).
46. R. Moessner, N. Morales-Durán, P. Surówka, P. Witkowski, *Phys. Rev. B* **100**, 155115 (2019).
47. P. Muralt, D. W. Pohl, in *Scanning Tunneling Microscopy* (Springer, 1986), pp. 252–254.
48. P. Muralt, H. Meier, D. W. Pohl, H. W. M. Salemink, *Appl. Phys. Lett.* **50**, 1352–1354 (1987).
49. C. S. Chu, R. S. Sorbello, *Phys. Rev. B* **40**, 5950–5955 (1989).
50. T. Druga, M. Wenderoth, J. Homoth, M. A. Schneider, R. G. Ulbrich, *Rev. Sci. Instrum.* **81**, 083704 (2010).
51. J. R. Kirtley, S. Washburn, M. J. Brady, *Phys. Rev. Lett.* **60**, 1546–1549 (1988).
52. K. H. Bevan, *Nanotechnology* **25**, 415701 (2014).
53. D. K. Morr, *Phys. Rev. B* **95**, 195162 (2017).
54. B. G. Briner, R. M. Feenstra, T. P. Chin, J. M. Woodall, *Phys. Rev. B* **54**, R5283–R5286 (1996).
55. R. Landauer, *IBM J. Res. Develop.* **1**, 223–231 (1957).
56. S.-H. Ji *et al*., *Nat. Mater.* **11**, 114–119 (2012).
57. F. Giannazzo, I. Deretzis, A. La Magna, F. Roccaforte, R. Yakimova, *Phys. Rev. B* **86**, 235422 (2012).
58. W. Wang, K. Munakata, M. Rozler, M. R. Beasley, *Phys. Rev. Lett.* **110**, 236802 (2013).
59. P. Willke, T. Druga, R. G. Ulbrich, M. A. Schneider, M. Wenderoth, *Nat. Commun.* **6**, 6399 (2015).
60. K. W. Clark *et al*., *ACS Nano* **7**, 7956–7966 (2013).
61. A. Sinterhauf *et al*., *Nat. Commun.* **11**, 555 (2020).
62. A. De Cecco *et al*., *Nano Lett.* **20**, 3786–3790 (2020).
63. J. P. Pelz, R. H. Koch, *Phys. Rev. B* **41**, 1212–1215 (1990).
64. J. Lee *et al*., *Nat. Phys.* **12**, 1032–1036 (2016).
65. J. Velasco Jr. *et al*., *Nano Lett.* **18**, 5104–5110 (2018).
66. B. Brun *et al*., *Phys. Rev. B* **100**, 041401 (2019).
67. See supplementary materials.
68. R. S. Sorbello, *Phys. Rev. B* **23**, 5119–5127 (1981).
69. R. S. Sorbello, C. S. Chu, *IBM J. Res. Develop.* **32**, 58–62 (1988).
70. H. Guo, E. Ilseven, G. Falkovich, L. Levitov, arXiv:1612.09239 [cond-mat.mes-hall] (2017).
71. C. Gutiérrez *et al*., *Science* **361**, 789–794 (2018).
72. E. A. Quezada-López *et al*., *Nanomaterials* **10**, 1154 (2020).
73. W. A. Behn *et al*., *Nano Lett.* **21**, 5013–5020 (2021).
74. J. A. Støvneng, P. Lipavský, *Phys. Rev. B* **42**, 9214–9216 (1990).
75. J. Park, G. He, R. M. Feenstra, A.-P. Li, *Nano Lett.* **13**, 3269–3273 (2013).
76. A. Lucas, *Phys. Rev. B* **95**, 115425 (2017).
77. S. S. Pershoguba, A. F. Young, L. I. Glazman, *Phys. Rev. B* **102**, 125404 (2020).
78. S. Li, M. Khodas, A. Levchenko, *Phys. Rev. B* **104**, 155305 (2021).
79. J. Geurs *et al*., arXiv:2008.04862 [cond-mat.mes-hall] (2020).
80. Z. J. Krebs *et al*., Imaging the breaking of electrostatic dams in graphene for ballistic and viscous fluids, version 1, Zenodo (2022); https://doi.org/10.5281/zenodo.7314592.

ACKNOWLEDGMENTS

The authors thank A. Marguerite for stimulating discussions. **Funding:** Funding was provided by US Department of Energy, Office of Science, Basic Energy Sciences (BES) Program for Materials and Chemistry Research in Quantum Information Science award DE-SC0020313 (Z.J.K., K.J.S., and A.L.); Office of Naval Research award N00014-20-1-2356 (W.A.B. and V.W.B.); National Science Foundation grant DMR-1653661 (S.L.); University of Wisconsin Materials Research Science and Engineering Center grant DMR1720415; Elemental Strategy Initiative, MEXT, Japan, grant JPMXP0112101001 (K.W. and T.T.); and JSPS KAKENHI grants JP19H05790 and JP20H00354 (K.W. and T.T.). **Author contributions:** Z.J.K. and W.A.B. performed all STP measurements and data analysis. K.J.S. fabricated the graphene devices. K.W. and T.T. grew the high-quality hBN crystals used in all graphene devices. S.L. and A.L. ran numerical simulations of electron fluid flow in graphene. V.W.B., Z.J.K., and W.A.B. conceived of the experiment and designed the measurement system. Z.J.K., S.L., and V.W.B. modeled the results using theoretical tools. Z.J.K., W.A.B., V.W.B., and S.L. wrote the manuscript. V.W.B. and A.L. supervised the experimental and theoretical aspects of the research, respectively. **Competing interests:** The authors declare that they have no competing interests. **Data and materials availability:** All data and files used to generate the results of this article—experimental and theoretical—can be found in Zenodo (*80*).

SUPPLEMENTARY MATERIALS

science.org/doi/10.1126/science.abm6073
Materials and Methods
Supplementary Text
Figs. S1 to S8
References (*81*–*84*)

Submitted 29 September 2021; accepted 24 January 2023
10.1126/science.abm6073